Spikes

bubbles

Highlighting research from the group of Dr Kun Xue at the State Key Laboratory of Explosion Science and Technology

Dual hierarchical particle jetting of a particle ring undergoing radial explosion

Soft particle rings subjected to radially divergent shock waves display an emergent dual hierarchical jetting pattern, consisting of distinct internal and external jetting structures. The overall pattern shows a proportionate growth mode during the semi-steady growth regime. Xue *et al.* elucidate the distinct physics underpinning the internal and external jetting.

ROYAL SOCIETY
OF CHEMISTRY

rsc.li/soft-matter-journal

Dual hierarchical particle jetting of a particle ring undergoing radial explosion

Kun Xue,*[a] Kaiyuan Du, [ID][a] Xiaoliang Shi,[a] Yixiang Gan[b] and Chunhua Bai[a]

We study experimentally the formation of a dual hierarchical jetting pattern in dry dense particle media subjected to the radially divergent shock loadings in a radial Hele-Shaw cell. The distinct internal and external jetting patterns were formed on the internal and external surfaces of a ring at different times, respectively. The former features dozens of radially aligned fine filaments. By contrast, the latter consists of a large number of small spikes. Once the internal jets are fully developed, a novel proportionate growth is observed, in which distinguishable structures of the overall pattern all grow at the same rate until the interaction between the internal and external jets becomes significant, leading to the inversion of the internal jetting pattern. Although the external jetting is found to be an instability of a Rayleigh–Taylor (RT) type, the internal jetting exhibits a much delayed onset and slower early-stage growth compared with the RT instability, indicating different underlying physics.

1. Introduction

Particle jetting instabilities have been widely observed in events involving shock/explosive dispersal of granular materials, liquids and hybrid mixtures, such as volcanic eruptions, meteorite impacts, explosions of landmines, thermobaric explosion, dense inert metal explosion, *etc.*[1–9] Understanding the underlying physics of particle jetting has been an active area of research, which entails thorough knowledge of the jet formation process, specifically the jetting instability onset, and the spatiotemporal evolutions of the jetting structure as well.[3–10] The interior evolution of granular media is difficult to access using three dimensional configurations in which spherical or cylindrical central bursters are surrounded by dry/wet particles.[1–5,9,10] More recently, Rodriguez *et al.* studied the jet wavelength selection using a semi-two-dimensional configuration in which a particle ring is confined inside a Hele-Shaw cell and impacted by weak divergent shock waves.[6–8] This prototype allows them to measure the jetting onset and track the changes in jet number after the instability onset.

However, little is known with regard to the evolution of the global features of the dual hierarchical jetting pattern after the jetting onset, especially the critical transformations of the global pattern and the growth rates of characteristic structures. These are the focuses of the present work.

Particle jetting bears striking configurational similarities with the "granular fingering", which has been widely observed

in experiments of air injection, or fluid/particle invasion into granular media, or particle-laden flows in Hele-Shaw cells.[11–15] Granular fingering, regardless of taking forms of fractal-like patterns or "stubby" fingers, is basically an instability of the Saffman–Taylor type, in which the coupled fluid–grain displacement process or shear-induced particle migration is the key defining event.[11,13,14,16] By contrast, it is the shock interaction with granular media rather than the hydromechanical coupling that dominates the particle jetting, since the characteristic timescale of the particle jetting is consistent with the shock interaction, several orders of magnitude smaller than that of hydromechanical coupling.[3–5,9,10] Therefore the particle jetting mechanism is fundamentally different from the viscous particle fingering.

Another worth-noting instability is the Rayleigh–Taylor (RT) and Richtmyer–Meshkov (RM) instability.[17–19] The RT instability occurs when a light fluid accelerates into a heavy fluid, or equally a heavy fluid decelerates into a light fluid. The RM instability arises from the interface between the two fluids subjected to an incident shock. The RT and RM instability can well account for the explosive dispersed fluid jetting,[5,18,20] and long have been argued as candidate mechanisms governing the particle jetting, despite several non-trivial challenges.[3–5] In the present work, we attempt to elucidate the plausibility and inadequacies of the RT and RM instability applied to the particle jetting.

Shock induced dual particle jetting confined in a Hele-Shaw cell is investigated in the present work. The internal jetting onset, when a circular inner surface develops into dozens of small finger-like protrusions, occurs much earlier than the external jetting onset, at which a large number of fine pointy spikes emerge from the external surface. The later-stage growth

[a] *State Key Laboratory of Explosive Science and Technology,*
  Beijing Institute of Technology, Beijing, 100081, China. E-mail: xuekun@bit.edu.cn
[b] *School of Civil Engineering, The University of Sydney, Sydney, Australia*
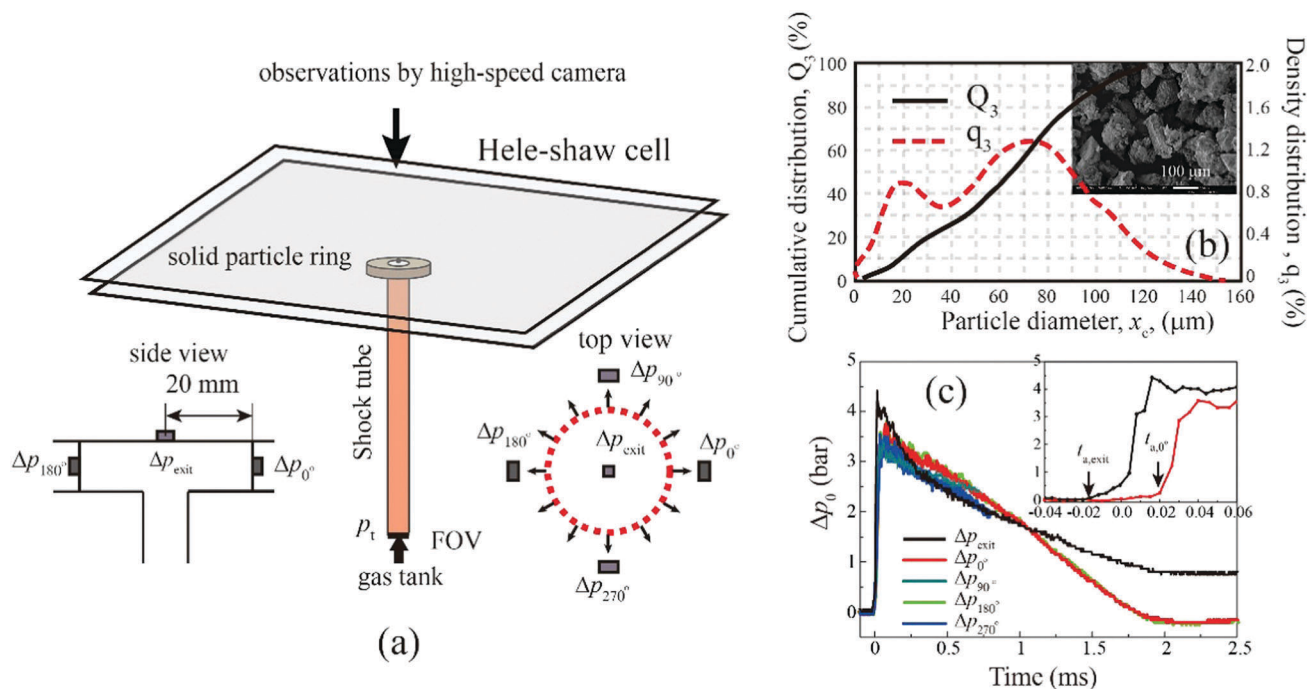
Fig. 1 (a) Schematic illustration of the experimental set-up. Left inset: Side view of the arrangement of pressure transducers; right inset: top view of the arrangement of pressure transducers. (b) Cumulative and density distributions of the particle diameter x_c, Q_3 and q_3, based on the volume. Inset: Scanning electronic image of the flour particles. (c) Pressure histories recorded at the exit of the shock tube and inside the Hele-Shaw cell. Inset: Zoomed leading edges of the pressure signals.

of internal jets and the early times growth of external jets can be well fitted by the RT instability growth model. The evolution of the overall hierarchical particle jetting pattern is found to be characterized by a novel proportional growth, in which the relative lengths of the characteristic structures are maintained throughout. The interaction between the internal and external jets increasingly retards the growth of the internal jets, eventually resulting in the inversion of the internal jetting pattern.

2. Experimental setup

The semi-two-dimensional experimental setup consists of a radial Hele-Shaw cell and a vertical shock tube as schematized in Fig. 1(a). Two $560 \times 560 \times 15$ mm Plexiglass plates comprising the Hele-Shaw cell are maintained at a constant gap, $b = 4$ mm, by placing spacers with the exact same thickness around the edge. The vertical shock tube with an inner diameter of 10 mm is attached to the central hole at the bottom plate of the Hele-Shaw cell by means of a flange. The end of the shock tube is connected with a pressurized tank by a fast opening valve (FOV). Before the experiments, the exit of the shock tube and the bottom plate is

separated by an aluminum foil diaphragm. A concentric flour particle ring with an inner and outer diameter of 20 and 60 mm is disposed around the shock tube exit and confined inside the Hele-Shaw cell. The internal and external surfaces of the particle ring are free of casings. The statistical distributions of the diameters of flour particles are presented in Fig. 1(b), showing an average diameter of 63.65 μm (based on volume, the standard deviation is 30.56 μm). The high resolution scanning electronic image shown in the inset of Fig. 1(b) shows a "chunky" morphology of the flour particle covered by fine chipping. The material properties as well as the rheological properties of particles are given in Table 1. The geometrical and rheological properties of particles are measured using CAMSIZER XT® (Retsch Technology) and a FT4 Powder Rheometer (freeman technology), respectively.

Once the fast opening valve is opened, the pressurized gases contained in the tank burst into the shock tube, thrust out of the diaphragm at the exit and are vented into the circular space enclosed by the flour ring. Alongside the adiabatic expansion of the pressurized gases, the flour ring is expelled outward by the impulsive divergent shock loadings. Five Kistler pressure transducers, one mounted on the top plate right above the

Table 1 Material and rheological properties of flour particles, where d_p, ρ_p, ρ_b, MC(%d.b.), Φ and σ_Y denote the average particle diameter (in μm), the material density (in kg m^{-3}), the bulk density (in kg m^{-3}), the moisture content, the angle of internal friction and the unconfined yield strength, respectively

Particle	d_p (μm)	ρ_p (kg m^{-3})	ρ_b (kg m^{-3})	MC (%d.b.)	Φ	Cohesion (kPa)	σ_Y (kPa)
Flour	63.65	1500	550–620	8.9	28.75	1.35	4.56

center of the shock tube exit (Δp_{exit}), and the other four placed inside the Hele-Shaw cell with the same radii ($\Delta p_{0°}$, $\Delta p_{90°}$, $\Delta p_{180°}$, $\Delta p_{270°}$), record the overpressures therein as presented in Fig. 1(c). The side and top views of the arrangement of pressure transducers are shown in the left and right insets of Fig. 1(a) respectively. All overpressure profiles exhibit an impulsive pressure jump followed by a rapid pressure decrease within the duration of 3 μs. The shapes of pressure signals at the tube exit (Δp_{exit}) and inside the Hele-Shaw cell ($\Delta p_{0°}$, $\Delta p_{90°}$, $\Delta p_{180°}$, $\Delta p_{270°}$) are quite similar, with the exception that the peak overpressure of Δp_{exit} is slightly higher than others. Note that the pressure signals at different locations inside the Hele-Shaw cell agree well with each other, indicating a homogeneous divergent flow. Varying the pressure through the FOV, p_t, and/or the thickness of the aluminum foil diaphragm can change the peak overpressure at the exit of the shock tube, Δp_{max}. The Δp_{max} investigated in our work ranges from 1.52 bar to 6.67 bar. From the time interval between the arrival times of Δp_{exit} and $\Delta p_{0°}$ (see the inset of Fig. 1(c)), we can derive the Mach number of the incident wave, which is found to range from 1.07 to 1.48.

The flow velocities inside the Hele-Shaw cell are difficult to access in this compact apparatus. We instead performed hydrodynamic simulations using the identical geometry to derive the flow velocities. The details of numerical simulations are presented in Appendix I. With the peak overpressure of Δp_{exit} varying from 1.5 to 7 bar, the peak flow velocity inside the Hele-Shaw cell, v_g, varies from 110 to 180 m s^{-1}. The order of magnitude of particle velocities, v_p, are $O(10^1–10^2)$ m s^{-1}, which are measured from the trajectories of the internal surfaces of rings as will be discussed below. The particle Reynolds number is defined as

$$\mathrm{Re} = \frac{|v_g - v_p|d_p}{\nu_g} \qquad (1)$$

where ν_g is the viscosity of gases. Substituting the values of respective variables, the order of magnitude of Re is $O(10^1–10^2)$.

The shock dispersal of the particle ring is recorded using a high-speed camera (Photron SA5) with a frame rate of 10 000 f s^{-1}.

3. Results

3.1 Overall development of the emergent dual jetting pattern

A sequence of key events during the shock dispersal of flour rings remains consistent throughout the investigated range of Δp_{max}. We thus give a detailed account of a typical particle jetting in the case with $\Delta p_{max} = 1.74$ bar.

Upon the release of the pressurized gases through the exit of the shock tube, an incident shock wave immediately transmits into the particle ring and compresses the particles in its wake, resulting in a 10% to 35% increase in the packing density when the incident wave leaves the external surface of the ring. At $t \sim 0.7$ ms, the initially smooth internal surface of the ring becomes recognizably perturbed, dozens of needle-like crevices regularly spaced along the inner perimeter. At the instability onset, the inner radius of the ring is almost one and a half times the initial one. The high-speed photos presented in Fig. 2(a)–(e) record the subsequent jetting pattern formation and its dramatic evolution. The initially narrow crevices quickly open up, forming finger-like channels with rounded cusps as shown in Fig. 2(a). Alongside the radial advance, the width of the channels increases upon erosion due to the intense gas flux inside the channels. These channels are referred to as internal jets. A well-defined jetting pattern is soon formed with persistent features. The envelope of the internal jets comprises dozens of radially aligned filaments connecting by the wide and rounded
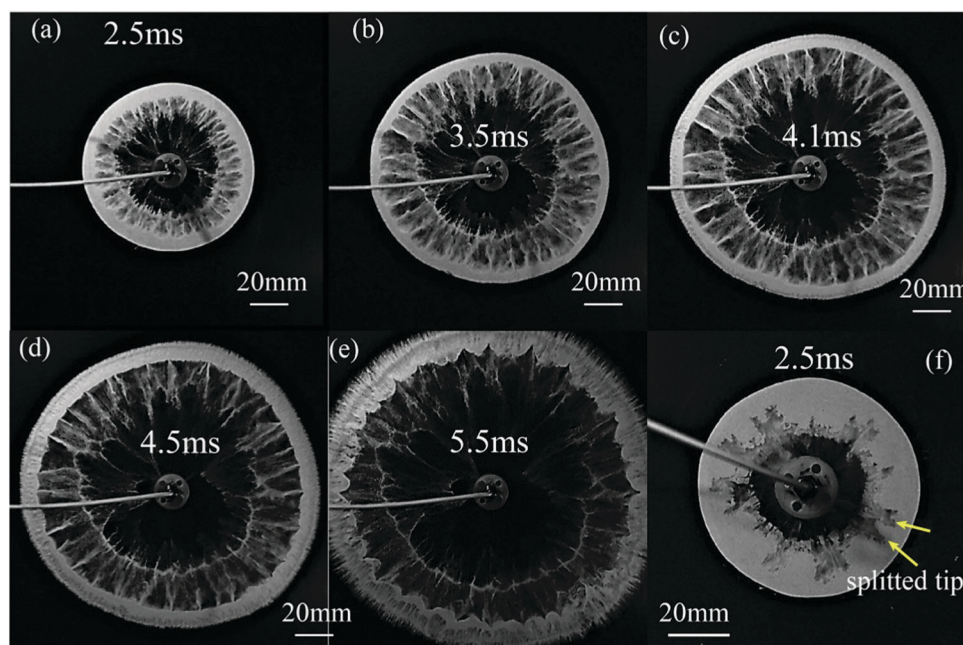

Fig. 2 (a–e) High-speed photos of the shock dispersal of the flour ring with $\Delta p_{max} = 1.74$ bar. (f) High-speed photo of the shock dispersal of the quartz sand ring with $\Delta p_{max} = 1.62$ bar.
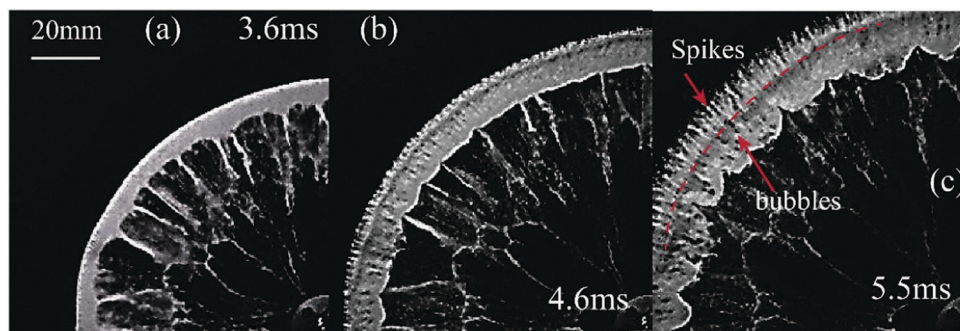
Fig. 3 Close-up visualization of the particle ring subjected to the shock loading with Δp_{max} = 1.74 bar before (a) and after (b and c) the external instability onset.

jet cusps (see Fig. 2(b)). What is worth noting is that the external surface remains unperturbed in this stage. Until $t \sim 4$ ms, the external surface of the ring suddenly becomes fuzzy, smeared by a large number of small perturbations (see Fig. 2(c)). Note that there still exists some distance between the cusps of internal jets and the external surface. The external instabilities rapidly grow into well-separated spike-like jets which simultaneously protrude outwards and extend inwards (see Fig. 2(d)). As the cusps of internal jets approach the external surface, they are progressively flattened with the radial advance significantly stalled. As a result, the initially convex cusps of internal jets get inverted and even become concave (see Fig. 2(d) and (e)). Eventually it is the ligaments rather than the cusps of internal jets themselves that penetrate the external surface (see Fig. 2(e)).

The close-up visualization of the particle ring before and after the appearance of the external jets (see Fig. 3) reveals how a complex external jet structure comes about. While the outmost layers of particles are ejected from the bulk, forming a large number of fine spikes, outside air is entrained into bulk so that tiny air pockets are deposited at the roots of the outward-going spikes (see Fig. 3(b) and (c)). A noticeable ridge

is formed between the ejecting spikes and an interior void ridden band.

The particle ejecta combined with the pockets of entrained air constitutes an increasingly thick "buffer band" which substantially retards the advance of the internal jets (see Fig. 3(b) and (c)). As the internal jets transverse the "buffer band", tiny bubbles acting like narrow air ducts effectively disintegrate the cusps of internal jets (see Fig. 3(c)), thereby dissipating the kinetic energy of internal jets. By contrast, the thin coherent ligaments between jet cusps retain their momentum and subsequently penetrate the external surface, leading to an inverted jetting pattern (see Fig. 2(e) and 3(c)). Actually the surviving jets which penetrate the external surface coincide with the initial ligaments of the internal jets.

The sequence of key defining events aforementioned is illustrated in Fig. 4. Fig. 4(a) and (b) show the well-defined filamentary radial internal pattern and the delayed occurrence of the external instability, respectively. The interaction between the internal and external jets, or equivalently how the ejecta-bubble complex structure brings about the inversion of the internal jetting pattern, is illustrated in Fig. 4(c) and (d).
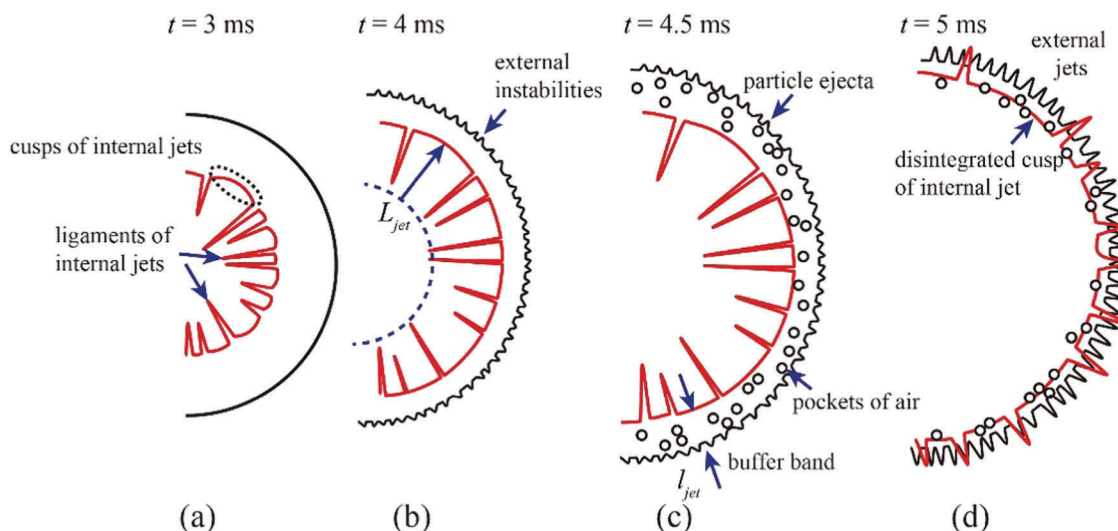

Fig. 4 Schematic illustration of the formation and evolution of the dual particle jetting pattern. The red and black lines represent the envelopes of the internal and external jets, respectively.
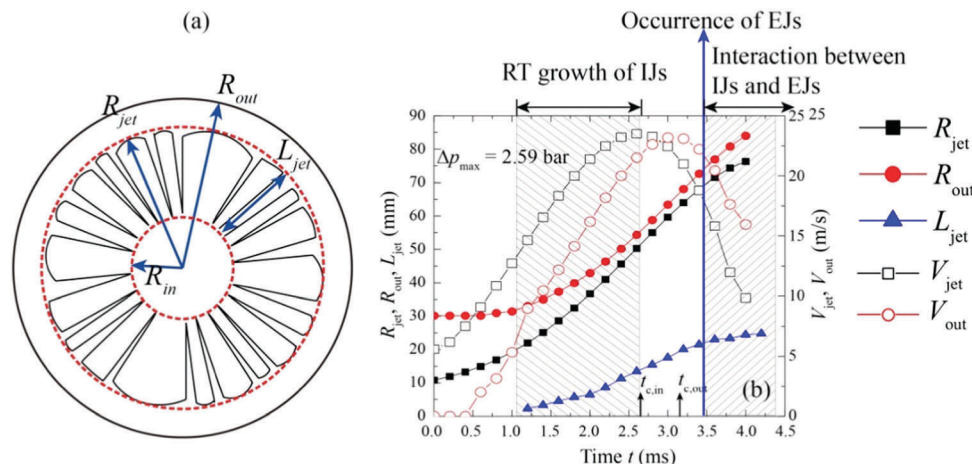
Fig. 5   (a) Determination of the characteristic length scales defining the large-scale jetting pattern, namely L_{jet}, R_{in}, R_{jet}, and R_{out}. (b)Temporal variations in R_{jet}, R_{out}, L_{jet}, and velocities of R_{jet} and R_{out} (V_{jet} and V_{out}) as well for the case with Δp_{max} = 2.59 bar. IJs: internal jets; EJs: external jets. $t_{c,in}$ and $t_{c,out}$ denote the acceleration-to-deceleration transition times of the internal and external perimeters, respectively.

3.2   Growth modes of internal and external jets

The growth of the dual jetting pattern after the instability onset is to be quantified by the increase rates of the internal and external jet lengths, L_{jet} and l_{jet}. L_{jet} corresponds to the distance between the cusps of jets and the ends of ligaments, equally the width of an annular gas–particle mixing region as indicated in the inset of Fig. 4(b). L_{jet} is then calculated from two characteristic length scales, the radius of the smallest circle that encloses all cusps of internal jets, R_{jet}, and the radius of the largest circle completely inscribed in the polygon whose vertices are ends of jet ligaments, R_{in}, $L_{jet} \equiv R_{jet} - R_{in}$. L_{jet}, R_{jet}, R_{in}, as well as the radius of the external perimeter, R_{out}, are illustrated in Fig. 5(a). l_{jet} refers to the thickness of the "buffer band", namely the "spike-bubble" complex structure, as indicated in the inset of Fig. 4(c).

The growth of L_{jet} and l_{jet} are closely correlated with the trajectories of the internal and external perimeters. Since the internal surface quickly becomes perturbed, the smallest circle that encloses all cusps of internal jets is instead regarded as the instantaneous internal surface as illustrated in Fig. 5(a). Fig. 5(b) plots the growth of L_{jet} against the temporal variations in the radii of internal and external surfaces, R_{jet} and R_{out}. The evolutions in expansion rates of R_{jet} and R_{out}, denoted by V_{jet} and V_{out}, respectively, are also plotted in Fig. 5(b). The internal and external surfaces both undergo an acceleration phase followed by a deceleration phase. The end of the internal surface acceleration, $t_{c,in}$, is prior to that of the external surface, $t_{c,out}$, by an interval less than 0.5 ms, which is the case throughout the investigated range of Δp_{max}.

The acceleration of the internal surface implies that the inside gases (lighter fluid) accelerates into granular media (heavier fluid). In this case, the perturbations in the inner interface will evolve and generally grow with time leading to a typical RT instability. Since the measurable value of L_{jet} is well beyond the initial linear regime of perturbations, the growth of L_{jet} should be driven by the turbulent mix of the interface.

Mikaelian proposed a simple model to describe the turbulent mixing width, h, in the cylindrical geometry if the acceleration of the interface is unchanged,[19]

$$h = \frac{cAgt^2}{15}\left[\frac{3}{2} + \frac{4R_0}{R} + \frac{2R_0}{R - R_0}\ln\left(\frac{R}{R_0}\right)\right], \qquad (2)$$

where c is a constant, g is the interface acceleration, A is the Atwood number across the interface, and R and R_0 are the instantaneous and initial radii of the cylindrical interface, respectively. A is defined as

$$A = \frac{\rho_2 - \rho_1}{\rho_1 + \rho_2}, \qquad (3)$$

where ρ_1 and ρ_2 are post shock densities across the interface. In our cases, ρ_1 and ρ_2 correspond to the densities of pressurized gases and shocked granular media. Since ρ_2 ($\sim O(10^3)$ kg m^{-3}) is three orders of magnitude larger than ρ_1 ($\sim O(10^0)$ kg m^{-3}), it is reasonable to assume $A \approx 1$.

Except the initial transient times and short duration prior to the acceleration-to-deceleration transition, the acceleration of the internal surface approximately remains constant (see Fig. 5(b)). Thus we attempt to fit the experimental data of L_{jet} during the acceleration phase using eqn (2). By adjusting the constant c, the experimental data agree and fit well with the correlation given in eqn (2) as suggested in Fig. 6(a).

The acceleration of the external surface corresponds to the granular media (heavier fluid) accelerating into air (lighter fluid), which retards the growth of any perturbations in the external surface. This stabilization effect accounts for the external surface remaining intact throughout the acceleration phase. When the expansion of the external surface begins to decelerate, which is equivalent to the outside air accelerating into the granular media, the perturbations that have been suppressed previously start to grow. The growth of the external jets, l_{jet}, is plotted in Fig. 6(b). At the first instants of the external surface deceleration, the interface velocity remains nearly constant;
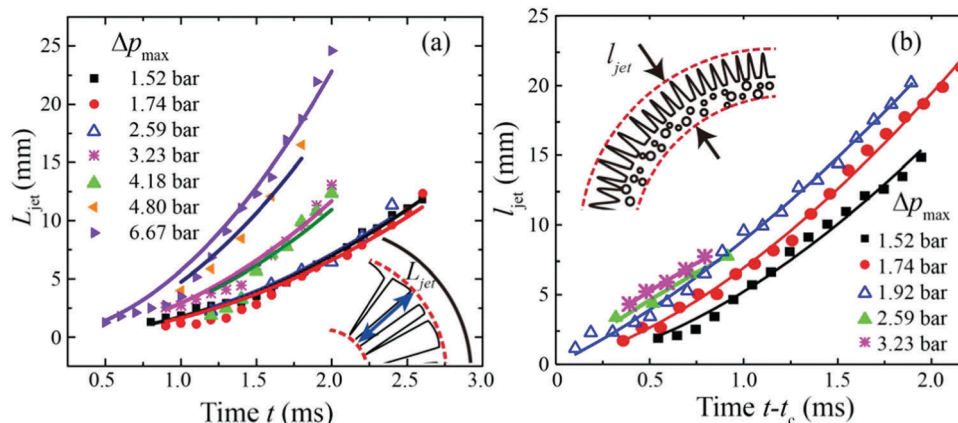
Fig. 6 Experimentally observed growth of the internal (a) and external jets (b) represented by scatter symbols *versus* the jet growth predicted using eqn (2) (a) and eqn (6) (b) represented by solid curves for cases with varying Δp_0.

however, after approximately 0.5 ms its variation becomes considerably larger. Thus the growth of l_{jet} results from the linear as well as the non-linear (turbulent mixing) regime of RT instability. When the motion of the interface is given by

$$R = R_0 + \dot{R}_0 t, \tag{4}$$

the magnitude of perturbations, $\eta(t)$, grows linearly with time[19]

$$\eta(t) = \eta_0 + \dot{\eta}_0 t \frac{R_0}{R}. \tag{5}$$

The experimentally observed external jet length, l_{jet}, does initially grow linearly with time and then its growth is increasingly dominated by the quadratic law (see Fig. 6(b)). The growth of l_{jet} is thus to be fitted by the correlation incorporating both linear and quadratic laws

$$
\begin{aligned}
l_{jet}(t) = {} & b \cdot \left(t - t_{c,out}\right) \frac{R_{out,c}}{R_{out}} + \frac{c g_{out}\left(t - t_{c,out}\right)^2}{15} \\
& \times \left[\frac{3}{2} + \frac{4 R_{out,c}}{R_{out}} + \frac{2 R_{out,c}}{R_{out} - R_{out,c}} \ln\left(\frac{R_{out}}{R_{out,c}}\right)\right],
\end{aligned}
\tag{6}
$$

where $R_{out,c}$ is the radius of the external surface at $t = t_{c,out}$, g_{out} is the deceleration of the external surface after $t_{c,out}$, b and c are adjustable constants. The growth of l_{jet} is found to be in a good

agreement with eqn (6). Detailed fitting procedures of L_{jet} and l_{jet} are given in Appendix II.

Despite the late stage growth of internal jets well resembling the turbulent mixing of the unstable interface as dictated by the RT instability, the initiation and early times growth of internal jets significantly deviate from the predictions of the RT instability. It takes quite a while for the perturbations in the internal surface to set in after the acceleration of the internal surface commences. Besides, it takes double or even triple the time for the internal jets to growth into the same recognizable length as it does for the external jets (compare Fig. 6(a) and (b)). More discussions regarding the initiation of internal jetting are presented in Section 4.

3.3 Proportionate growth of the overall jetting pattern

The overall shape of the dual jetting pattern changes if some characteristic structures grow faster than others. Thus it is necessary to examine the growth of structural features relative to each other as the expansion of the ring proceeds. We define four characteristic length scales representative of signature features as illustrated in Fig. 5(a), namely R_{out}, R_{jet}, R_{in}, and L_{jet}. Bischofberger *et al.* adopted a similar approach to quantify the growth pattern of viscous fluid fingering.[21–23]

Specifically we examine the variations in ratios between two of the four characteristic length scales as a function of R_{out}. Fig. 7(a)–(c) show the variations in R_{jet}/R_{out}, L_{jet}/R_{out} and L_{jet}/R_{in}
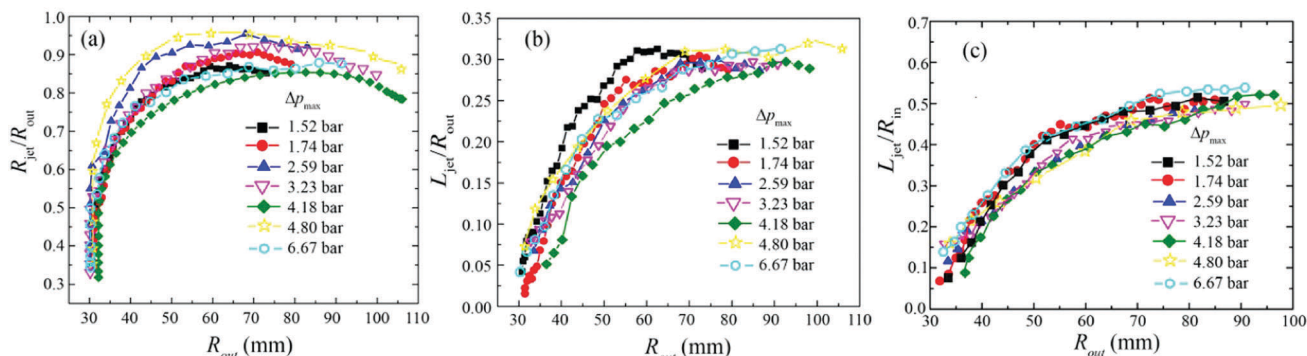

Fig. 7 Variations in R_{jet}/R_{out} (a), L_{jet}/R_{out} (b) and L_{jet}/R_{in} (c) with increasing R_{out} for cases with varying Δp_{max}.

with increasing R_{out} for cases with varying Δp_{max}, respectively. What is most striking is that all data seem to fall into a narrow band regardless of Δp_{max} in each figure. Another point worth noting is that all three ratios undergo an initial fast growth and gradually transit to a steady-state regime despite the fact that the ratio R_{jet}/R_{out} enters into a stable growth phase much earlier than the other two ratios. Whatever value Δp_{max} is, the converged values of R_{jet}/R_{out}, L_{jet}/R_{out} and L_{jet}/R_{in} in the steady-state regime are in the range of 0.86–0.92, 0.28–0.31 and 0.47–0.52, respectively. The noticeable tail-down of R_{jet}/R_{out} and L_{jet}/R_{out} at the very late times are caused by the interaction between the internal and external jets.

The prominent steady-state growth of R_{jet}/R_{out}, L_{jet}/R_{out} and L_{jet}/R_{in} guarantees that the relative lengths of global features remain consistent after an initial transient growth phase. This type of growth, in which a pattern is composed of distinguishable structures all growing at the same rate, is called proportionate growth.[22] The top row of Fig. 8 show the snapshots of the shock dispersed ring subjected to different Δp_{max} and taken at different times. Zooming out the left bottom squares of rings in these three snapshots, we can get zoomed images with the same outer radius (see the bottom row of Fig. 8). Although these zoomed images have detectable differences in terms of the spacing of jets and the mixing extent in the mixing regions, the internal jets grow in proportion to the internal and external radius, R_{jet} and R_{out}, respectively. The respective proportionality remains constant throughout the proportionate growth and is unvaried with varying Δp_{max}.

The proportionate growth observed in our study, although short-lived due to the interaction between the internal and external jets in late times, is quite rare in the pattern formation domain. With regard to the interface instability, to our knowledge, only the group of Bischofberger reported the proportionate growth in the viscous fingering instability of systems of two miscible fluids with a high enough viscosity ratio.[22,23] Opposed to the tip splitting or side-branching occurring in common viscous fingering, such system becomes unstable only once, to produce distinguishable structures, but then turns off the instability mechanism so that no further generations can develop. A proportionate growth sets off. There exists a clear parallel between the proportionate growth in the viscous fingering instability and that in the particle jetting. The defining features of the (internal) jetting pattern are maintained throughout once the structures are fully developed. The instability mechanism in the flour jetting is again initiated only once. However this proportionate growth is not universal in the particle jetting instability. Contrasting with the dense filamentary radial pattern formed in the flour ring, the jetting instability in the quartz sand ring takes the form of sparsely spaced branched fingers as shown in Fig. 2(f). More importantly, the tip-splitting occurs frequently in the quartz sand jetting, indicating a totally different growth mode other than the proportionate growth. Understanding the changes of the jetting instability mode with the materials should be the subject of the follow-up work.

4. Discussions

As has been revealed in Section 3.2, the external particle jetting can be regarded as an instability of the RT type in the granular
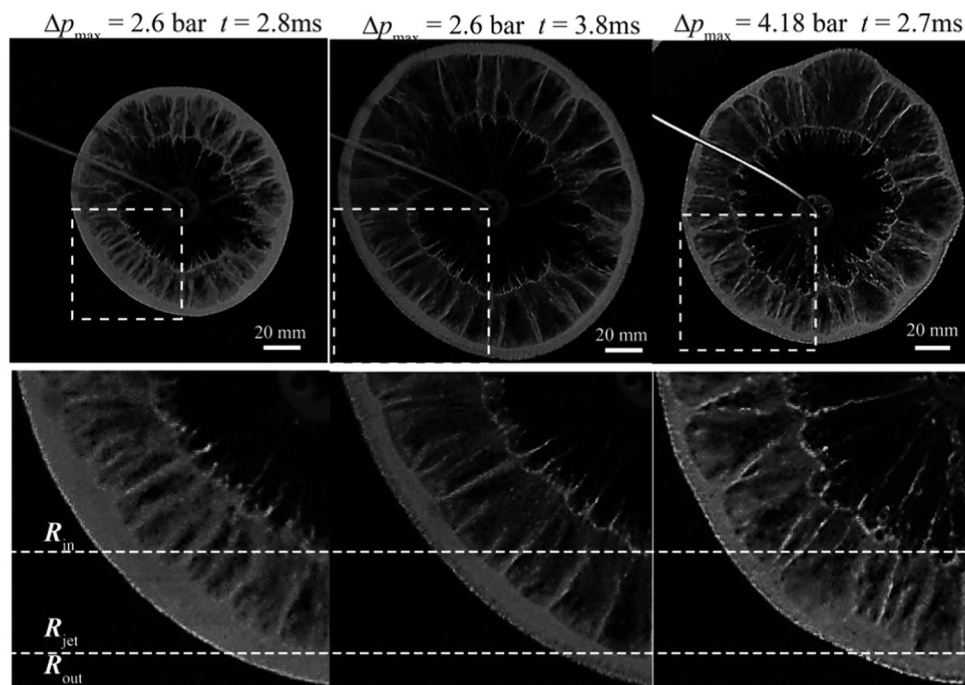

Fig. 8   Top row: High-speed photos of particle ring during the steady-state growth stage subjected to shock loading with different Δp_{max}; bottom row: zoomed images of the left bottom squares of rings in the top raw pictures.

media: first, the instability onset of the external surface closely ensue the acceleration-to-deceleration transition after which the air accelerates into the particles; second, the external jets exhibit signature "spike and bubble" structure;[17,19] third, the growth of external jets agrees well with the growth model of RT instability which incorporates both linear and nonlinear regimes.[17,19] Nevertheless the selection mechanism of the dominant azimuthal dimensional wavelength of external jets, or equivalently the characteristic spacing between jets, s_{jet}, cannot be understood in light of the most unstable wavelength of RT instability. With the surface tension stabilizing the short wavelengths, the most unstable wavelength of RT instability is expected to be of the order of

$$\lambda = \frac{2\pi}{\sqrt{\rho A_0/\alpha}}, \tag{7}$$

where A_0 is the acceleration of the interface and α is the surface tension.[18] In our cases, $\rho \sim 600$ kg m^{-3}, $A_0 \sim 10$ m s^{-2}, and $\alpha \sim 10^{-6}$ mJ m^{-2}.[12] Substituting these values of variables into eqn (7), one finds that the λ is of the order of 10^0 μm which is much smaller than the average diameter of particles, d_p. Actually we found that the average spacing of external jets, s_{jet}, is in the range of 1.7–2.6 mm, much larger than d_p. The failure of RT instability theory in accounting for the characteristic spacing between jets implies that there ought to be some forces instead of the surface tension to regularize the behavior of the short waves.

Likewise, RT instability theory also fails to account for the wavelength selection of internal jets. The average spacing of internal jets, S_{jet}, varies from 3.6 to 4.5 mm for the investigated range of Δp_{max}, much larger than s_{jet}, suggesting a distinct wavelength selection. Note that S_{jet} and s_{jet} are derived from the perimeters of internal and external surfaces at respective instability onset divided by the respective jet number, respectively.

The wavelength selection mechanism of the internal jets is especially important, since it not only determines the spatial jetting structures, but also controls whether the proportionate growth of the overall pattern occurs or not. Opposed to the hydrodynamic interface instability, such as RT and RM instability, increasing body of both experimental and numerical evidences suggests that the initiation of the (internal) particle jetting may well arise from a certain particle agglomeration despite the causes are still debatable.[6,24,25]

Our previous particle-scale simulations based on the discrete element method (DEM) found that the precursors of internal jets originate from the heterogeneities introduced by the heterogeneous force structure, which dictates a unique manner of momentum/energy transmission in granular materials.[26] The wavelength and shape of jets decidedly are prescribed by the intrinsic structure of force chains which mainly depends on the local packing arrangement and material properties as well.[26] Recent studies by Clark et al. found that the force structure in striker impacted particle bed changes dramatically with the "effective hardness" of the particle material.[27] As the particle material becomes increasingly softer, a sparse, chain-like force structure progressively evolves into a dense network with

a well-defined front. Our DEM simulations also depict an analogous picture when particle rings are to be dispersed by divergent impulsive loading (not presented here). The dense network of force chains in soft particles generate a population of evenly spaced instabilities which grow in a balanced manner. By contrast, a sparse, chain-like force structure in hard particles gives rise to a handful of singularly strong instabilities wherein the ramification occurs. These findings can well account for the district jetting patterns observed in flour and quartz sand particles, which represent the typical soft and hard particles. Meanwhile the proportionate growth of the overall pattern tends to be switched off as the particles become harder. Quantitatively characterizing the correlation between the jetting pattern and the "effective hardness" of the particle material, or more generally the force structure, should be the subject of the follow-up work.

5. Conclusions

Dual hierarchical particle jetting arises from the instabilities of the internal and external surfaces of the particle ring, respectively, which occur at different times and exhibit remarkably different features. The external jetting is an instability of the RT type, while the wavelength selection mechanism should incorporate some forces instead of the surface tension to stabilize the short wavelengths. RT or RM instability however is inadequate to account for the initiation and early times growth of internal jets, although their late times growth is governed by the turbulent mixing of the RT perturbed interface.

Once the internal jets fully set in, the evolution of the overall jet pattern is dominated by the proportionate growth until the interaction between the internal and external jets becomes significant which leads to the inversion of the internal jetting pattern. The global features of pattern in terms of the relative lengths of the characteristic length scales persist throughout the growth of pattern and more strikingly remains consistent regardless of the peak overpressure we studied in the work. It is important to note that the proportionate growth is the growth mode inherent to soft particles, which does not exist in hard particles.

Conflicts of interest

There are no conflicts to declare.

Appendix I

The flow profile inside the Hele-Shaw cell is analyzed computationally using AUTODYN, a general-purpose transient nonlinear dynamics analysis software. The set-up of problem is identical to the one descried in Section 2. The corresponding computational multi-material Euler model is shown in Fig. 9. The lower part of the cylindrical tube with an inner diameter of 10 mm is filled with pressurized gases with the pressure p_t while other parts are filled with air. A particle ring with an inner- and outer-diameter of 20 and 40 mm is sandwiched
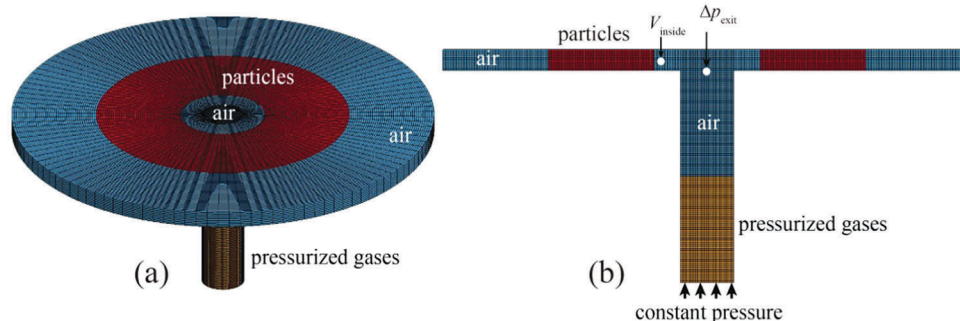
Fig. 9 (a) Computational sub-domains in the present work. (b) Locations of pressure and velocity gauges.

between the top and bottom plates of the Hele-Shaw cell with the centerline aligning with that of the shock tube. The "constant pressure" boundary condition is applied to the outer boundary of the pressurized gas filled portion. The "flow out" boundary conditions are applied to all air-filled portions of domain. The equation of the state of ideal gas is used for the pressurized gases and air. The behavior of the particle ring is described by the compaction model proposed by Laine and Sandvik used in AUTODYN. The values of all the material parameters for

pressurized gases, air and particles are available in the AUTODYN materials library and, hence, can be accessed by all licensed AUTODYN users.

The computed pressure history at the exit of the shock tube in the trial with $p_t = 2$ bar is shown in Fig. 10(a). The peak overpressure, Δp_{max}, is consistent with the experimental result. The subsequent fluctuations of Δp_{exit} are due to the confinement of the particle ring which is much stiffer than the actual material. Fig. 10(b) shows the temporal variations in gas velocity near the
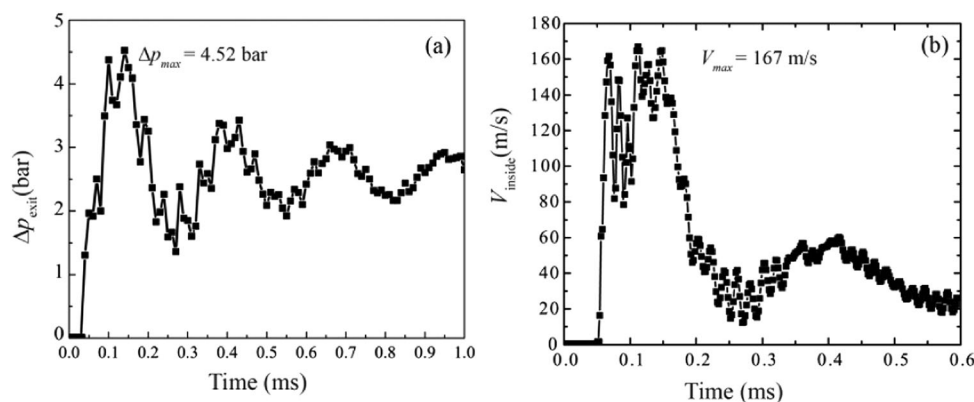

Fig. 10 Temporal variations in pressure at the exit of the shock tube (a) and velocity near the internal perimeter of the ring (b). The locations of the pressure and velocity gauges are shown in Fig. 9(b).
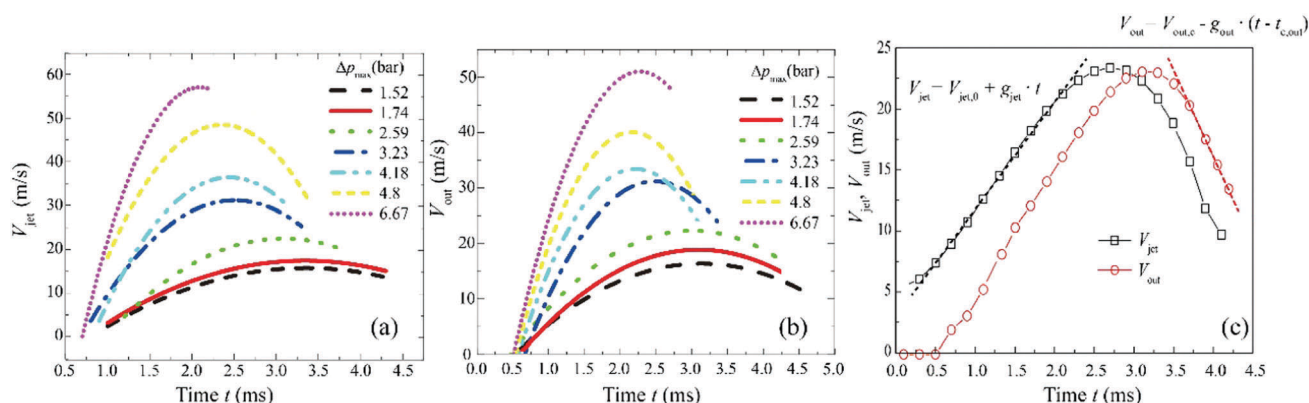

Fig. 11 Temporal variations in V_{jet} (a) and V_{out} (b) for cases with varying Δp_{max}. (c) Illustration of fitting the V_{jet} vs. t curve before $t = t_{c,in}$ and the V_{out} vs. t curve after $t = t_{c,out}$ using the linear equations, respectively, for the case with $\Delta p_{max} = 2.59$ bar.

Table 2 Values of g_{jet}, g_{out}, the adjustable constants c in eqn (1), b and c in eqn (2) derived from fitting the L_{jet} vs. t and the l_{jet} vs. t curves with eqn (2) and (4), respectively

		Constant in eqn (1)		Constants in eqn (4)	
Δp_{max} (bar)	g_{jet} (m s^{-2})	c	g_{out} (m s^{-2})	b	c
1.52	9.10	0.385	3.35	1.448	2.488
1.74	11.42	0.295	4.21	3.0680	2.2160
1.92	15.05	0.291	4.82	6.494	1.924
2.59	17.57	0.287	6.04	9.545	0.1776
3.23	24.24	0.241	12.15	10.43	0.0007396
4.18	32.21	0.170	13.88		
4.8	38.26	0.247	19.33		
6.67	62.54	0.268			

interior perimeter of the ring. The maximum velocity, V_{max}, is used to calculate the particle Reynold number defined in eqn (1).

Appendix II

We attempt to fit the growth of the internal and external jets with eqn (2) and (6), respectively. To obtain the g_{jet} of the internal surface before $t = t_{c,in}$ and g_{out} of the external surface after $t = t_{c,out}$, the curves of V_{jet} *versus* time before $t = t_{c,in}$ (see Fig. 11(a)) and V_{out} *versus* time after $t = t_{c,out}$ (see Fig. 11(b)) are fitted by linear functions as exemplified in Fig. 11(c). The values of g_{jet}, g_{out}, adjustable constant b and c in eqn (2) and (6) are given in Table 2 for varying Δp_{max}. The values of constant c in eqn (2) varies from 0.17 to 0.385, comparable to the range ($c \approx \sim 0.1$–0.14) observed in RM experiments. Since the experimental data of the external jet length for elevated Δp_{max} are limited to the initial linear growth regime, the nonlinear growth regime becomes negligible suggested by the quite small values of the proportionality of the nonlinear term, c.

Acknowledgements

References

1 C.-H. Bai, Y. Wang, K. Xue and L.-F. Wang, *Shock Waves*, 2018, DOI: 10.1007/s00193-017-0795-8.

2 L. F. David, G. Yann, P. Oren, G. Samuel and Z. Fan, *Phys. Fluids*, 2012, **24**, 091109.

3 A. Milne, C. Parrish and I. Worland, *Shock Waves*, 2010, **20**, 41–51.

4 A. M. Milne, E. Floyd, A. W. Longbottom and P. Taylor, *Shock Waves*, 2014, **24**, 501–513.

5 R. C. Ripley and F. Zhang, *J. Phys.: Conf. Ser.*, 2014, **500**, 152012.

6 V. Rodriguez, R. Saurel, G. Jourdan and L. Houas, *Phys. Rev. E: Stat., Nonlinear, Soft Matter Phys.*, 2013, **88**, 063011.

7 V. Rodriguez, R. Saurel, G. Jourdan and L. Houas, *Phys. Rev. E: Stat., Nonlinear, Soft Matter Phys.*, 2014, **90**, 043013.

8 V. Rodriguez, R. Saurel, G. Jourdan and L. Houas, *Shock Waves*, 2017, **27**, 187–198.

9 K. Xue, F. Li and C. Bai, *Eur. Phys. J. E: Soft Matter Biol. Phys.*, 2013, **36**, 1–16.

10 D. L. Frost, J. Loiseau, B. J. Marr and S. Goroshin, *AIP Conf. Proc.*, 2017, **1793**, 120020.

11 F. Xu, J. Kim and S. Lee, *J. Non-Newtonian Fluid Mech.*, 2016, **238**, 92–99.

12 X. Cheng, L. Xu, A. Patterson, H. M. Jaeger and S. R. Nagel, *Nat. Phys.*, 2008, **4**, 234.

13 F. K. Eriksen, R. Toussaint, A. L. Turquet, K. J. Måløy and E. G. Flekkøy, *Phys. Rev. E*, 2017, **95**, 062901.

14 H. Huang, F. Zhang, P. Callahan and J. Ayoub, *Phys. Rev. Lett.*, 2012, **108**, 258001.

15 J. Kim, F. Xu and S. Lee, *Phys. Rev. Lett.*, 2017, **118**, 074501.

16 F. Zhang, B. Damjanac and H. Huang, *J. Geophys. Res.: Solid Earth*, 2013, **118**, 2703–2722.

17 J. Ding, T. Si, J. Yang, X. Lu, Z. Zhai and X. Luo, *Phys. Rev. Lett.*, 2017, **119**, 014501.

18 B. H. Bang, C. S. Ahn, D. Y. Kim, J. G. Lee, H. M. Kim, Y. T. Jeong, W. S. Yoon, S. S. Al-Deyab, J. H. Yoo, S. S. Yoon and A. L. Yarin, *Phys. Fluids*, 2017, **29**, 049902.

19 K. O. Mikaelian, *Phys. Fluids*, 2005, **17**, 094105.

20 F. Zhang, R. C. Ripley, A. Yoshinaka, C. R. Findlay, J. Anderson and B. von Rosen, *Shock Waves*, 2015, **25**, 239–254.

21 I. Bischofberger, R. Ramachandran and S. R. Nagel, *Nat. Commun.*, 2014, **5**, 5265.

22 I. Bischofberger and S. R. Nagel, *Phys. Today*, 2016, **69**, 70–71.

23 I. Bischofberger, R. Ramachandran and S. R. Nagel, *Soft Matter*, 2015, **11**, 7428–7432.

24 A. N. Osnes, M. Vartdal and B. A. Pettersson Reif, *Shock Waves*, 2017, DOI: 10.1007/s00193-017-0778-9.

25 T. Xu, F.-S. Lien, H. Ji and F. Zhang, *Shock Waves*, 2013, **23**, 619–634.

26 K. Xue, L. Sun and C. Bai, *Phys. Rev. E*, 2016, **94**, 022903.

27 A. H. Clark, A. J. Petersen, L. Kondic and R. P. Behringer, *Phys. Rev. Lett.*, 2015, **114**, 144502.